Journal of Marine Science and Technology

Volume 27 | Issue 2 Article 7

FLAME AND FLOW CHARACTERISTICS OF A PLANE-JET FLAME MODULATED BY A V-SHAPED FLUIDIC OSCILLATOR

Ching Min Hsu
Department of Mechanical Design Engineering, National Formosa University, Yunlin, Taiwan, R.O.C,
cmhsu@nfu.edu.tw

Hsiu Feng Yang
Department of Mechanical Engineering, Taipei City University of Science and Technology, Taipei, Taiwan, R.O.C.

Yuan Xu Zhang
Department of Mechanical Design Engineering, National Formosa University, Yunlin, Taiwan, R.O.C.

Recommended Citation

Hsu, Ching Min; Yang, Hsiu Feng; and Zhang, Yuan Xu (2019) "FLAME AND FLOW CHARACTERISTICS OF A PLANE-JET FLAME MODULATED BY A V-SHAPED FLUIDIC OSCILLATOR," *Journal of Marine Science and Technology*: Vol. 27: Iss. 2, Article 7.
DOI: 10.6119/JMST.201904_27(2).0007
Available at: https://jmstt.ntou.edu.tw/journal/vol27/iss2/7

Journal of Marine Science and Technology, Vol. 27, No. 2, pp. 144-152 (2019)
DOI: 10.6119/JMST.201904_27(2).0007

FLAME AND FLOW CHARACTERISTICS OF A PLANE-JET FLAME MODULATED BY A V-SHAPED FLUIDIC OSCILLATOR

Ching Min Hsu[1], Hsiu Feng Yang[2], and Yuan Xu Zhang[1]

Key words: fluidic-oscillator burner, flame characteristics, flow field, PIV.

ABSTRACT

The characteristic flame behaviors and velocity fields of a plane-jet flame modulated by a fluidic oscillator were experimentally studied. The flame behaviors were observed by the traditional photographic technique. The time-averaged velocity fields of the jet flame were measured by a high-speed particle image velocimeter. The temperature distributions of the jet flame were measured by an R-type thermocouple. The pulsating reacting jets issued from the side slots of the fluidic-oscillator burner formed two diffusion flames. By observing the flame behavior at around burner exit, three characteristic flame modes: attached flame, transitional flame, and lifted flame, were identified in the domain of central jet Reynolds number and coflowing air jets Reynolds number. The time-averaged velocity field showed that a source point is formed in the wake of the target blockage. Above the source point, the flow goes downstream direction. Beneath the source point, the flow reverses toward upstream direction, and then forms a reverse flow region. Two adjacent vorticity-concentrated areas with opposite signs were formed around the region where the pulsating fuel jet interacts with the coflowing air jets. The increase of pulsating jet velocity asserted a large momentum impinging on the coflowing air jets, therefore caused the coflowing air jets to deflect toward transverse direction. The axial velocity, turbulence intensity, and temperature distributions of the lifted flame mode presented larger values than those of the attached flame and transitional flame modes.

Paper submitted 08/17/18; revised 11/23/18; accepted 03/15/19. Author for correspondence: Ching Min Hsu (e-mail: cmhsu@nfu.edu.tw).
[1] *Department of Mechanical Design Engineering, National Formosa University, Yunlin, Taiwan, R.O.C.*
[2] *Department of Mechanical Engineering, Taipei City University of Science and Technology, Taipei, Taiwan, R.O.C.*

I. INTRODUCTION

The plane jet is prevalent in a wide range of industrial applications, such as combustion, chemical mixing, heat transfer, and air conditioning (Sato, 1960; Gutmark and Wygnanski, 1976; Hussain and Clark, 1977; Namar and Otugen, 1988). The natural jet behaves strong axial momentum and weak transverse momentum, so that the breakup and mixing phenomena induced by the entrainment effect are not strong enough in industrial applications. The natural jet, therefore, usually requires improvements to enhance its transport properties in momentum, heat, and mass transfers. Several literatures investigate the effects of jet-exit aspect ratio (*AR*, defined as the ratio of slot length to slot width) on the flow properties of the plane jets, such as jet velocity decay and spreading, turbulence intensity, and entrainment (Quinn, 1992; Zaman, 1999; Mi and Nathan, 2005; Deo et al., 2007). The flow properties generated in the near field in turn influence the far field flow characteristics. Plane jets with low aspect ratios exhibit a slight increase in spreading when compared to the conventional circular nozzles. However, the noticeable enhancement of jet spreading and mixing may commence at $AR > 10$ (Zaman, 1999). The statistically two-dimensional mean velocity field exists for $AR \geq 30$ (Deo et al., 2007).

To enhance entrainment of a plane jet, a specially designed device, which commonly called the fluidic oscillator, was used to generate periodic oscillation of fluid flow without using any moving or deformed components when a steady fluid flow passes through it. The inherent instability characteristics of the jet fluid in the fluid oscillator were transformed from convectively unstable state to absolutely unstable state, because the impulse response induced by the transient disturbance became unbounded at all locations in a flow with absolutely unstable characteristics (Huerre and Monkewitz, 1985; Gad-el-Hak et al., 1998). Therefore, the flow characteristics such as the transient large-scale flow structures and the turbulence properties were modified. Depending on the formation mechanism of jet oscillation, fluidic oscillators were classified into two categories: one was pressure-feedback fluidic oscillator, and the other was jet-impingement fluid oscillator. The pressure-feedback fluidic oscillator used downstream jets—either as a pressure pulse or as an actual flow through feedback channels to induce oscillation of the upstream

jet (Trippetts et al., 1973; Yamasaki and Honda, 1981; Wang et al., 1998; Yamamoto et al., 1999). The jet-impingement fluidic oscillator induced the self-sustained transverse oscillation of a plane jet by using the characteristics of jet-impingement instability (Lin et al., 1993).

A V-shaped jet-impingement fluidic oscillator was developed and characterized by Huang and Chang (2005, 2007). The oscillations of the fluid flow were induced without using the feedback signal of the cavity pressure fluctuation. They observed the evolution process of the large-scale coherent flow structure and the turbulence properties of the transversely flapping jet flow generated by the jet-impingement fluidic oscillator. Their observations demonstrated that the self-sustained flapping jet in the cavity of the jet-impingement fluidic oscillator guided through two channels, bifurcated into two pulsatile jets, and issued alternately with inverse phase angles out to the wake of the fluidic oscillator. The two pulsatile jets issued alternately into the wake of the jet-impingement fluidic oscillator would merge into one pulsating free plane jet in the near downstream area and cause large turbulence and significant transverse dispersion of the axial momentum. Huang et al. (2013) and Yang et al. (2014a, 2014b) installed the V-shaped fluidic oscillator at the exit of a plane fuel jet to investigate the effects of pulsating jets on flame behavior and thermal characteristics of the plane jet flame. The pulsating jet flame had improved with a 45% length reduction and a 40% width gain when compared to a non-pulsating plane jet flame. The pulsating jet flames also presented higher temperature values and wider transverse distributions than the non-pulsating ones. However, at higher flow rates the flame was lifted, and had two flame branches near the base that merged higher up. The gap between the two divergent flames may have negative effect on combustion rate and efficiency.

According to Huang et al.'s and Yang et al.'s works (Huang et al., 2013; Yang et al., 2014a; Yang et al., 2014b), the fluidic oscillator could be used to increase the combustion intensity of plane-jet flame. They also demonstrated that the enhancement in the combustion may be attributed to the enhancement of jet fluid entrainment and mixing. However, little information on the characteristics of the velocity fields, vorticity contours, and distributions of mean velocity and turbulence intensities was found in the literatures. To extend Huang et al.'s work, the present study used a jet-impingement fluidic oscillator to investigate the flame and flow characteristics by flame visualization, particle image velocimetry (PIV), and temperature measurements of the plane jet flame. The flame behavior, time-averaged velocity fields, vorticity contours, and distributions of velocity, turbulence intensity, and temperature of the fluidic-oscillator burner were simultaneously presented and discussed.

II. EXPERIMENTAL METHODS

1. Fluidic-Oscillator Burner

Fig. 1 shows the schematic diagram of a fluidic-oscillator burner developed by Huang et al. (2012). The central jet fluid was propane, composed of 95% C_3H_8, 3.6% C_2H_6, and 1.5% C_4H_{10}. The propane gas passed through a pressure regulator, rotameter, cyclone particle generator, then flowed through a nozzle before injecting into a fluidic oscillator. The rotameter measured the averaged exit velocity of the central jet (u_c) which was the averaged exit velocity of the nozzle. The nozzle exit was a narrow slot. The width (d) and span length (s) of the nozzle exit were 2 mm and 165 mm, respectively.

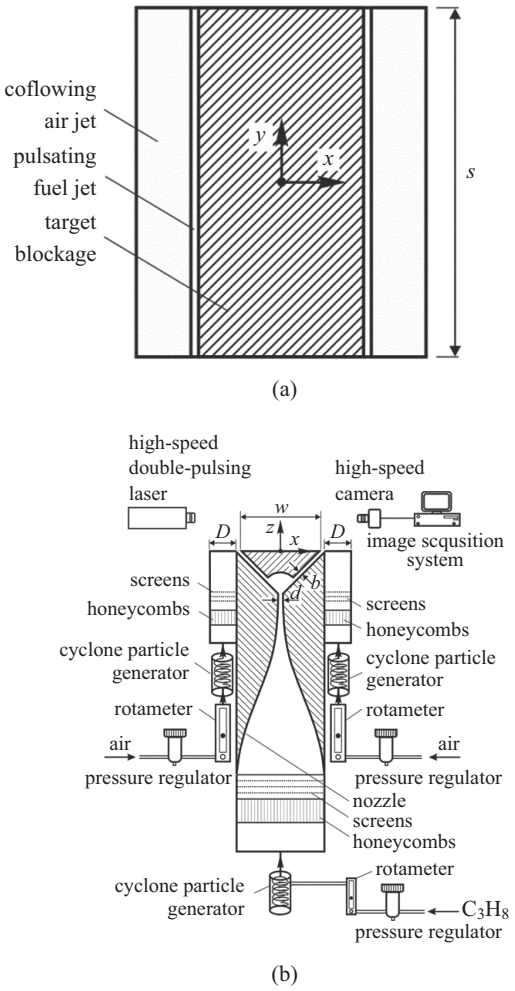

Fig. 1. Experimental setup.

A target blockage made of an isosceles right-angled triangular stainless steel block was installed above the nozzle exit. Its right-angled vertex was faced down and removed with a radius of R = 8 mm so that a concave surface facing downward was formed. The downstream width of the target blockage (W) was 35 mm. A cavity is enclosed between the nozzle exit and concave of target blockage. Two narrow inclined channels were formed between the side faces of target blockage and the inclined faces of the two metallic blocks. The width (b) and span length (s) of the inclined channels were 2 mm and 165 mm, respectively. A V-shaped fluidic oscillator including the cavity and the two channels was built in downstream region of the nozzle exit. When the dimensions of the fluidic oscillator and nozzle mentioned above were designed (Yang et al., 2014b), the central jet discharged

from nozzle exit impinged on the concave surface of target blockage, flapped back and forth transversely in the cavity, and ejected alternately out of the exits of the inclined channels. The pulsating jets under an isothermal condition in the wake region of the fluidic oscillator were obtained at $850 < Re_c < 3800$. The aspect ratio of the pulsating jets (s/b) was 82.5, which was significantly larger than a critical value of 30 proposed by Deo et al. (2007) for creating a statistically 2-D plane jet. Two channels with a width of $D = 11$ mm stood beside the pulsating jets to provide two coflowing air jets. The air fluid provided from the air tank passed through the pressure regulators, rotameters, cyclone particle generators, and then flowed through the channels. The averaged exit velocities of coflowing air jets were monitored by the rotameters. The Reynolds number of the jet flows is defined as follows.

$$Re_i = \frac{u_i L}{v_i} \tag{1}$$

where u_i is jet flow velocity, L is characteristic length, and v_i is kinematic viscosity of jet flow. The subscripts (i) for central fuel jet and coflowing air jets are c and a, respectively. The characteristic lengths of central fuel jet and coflowing air jets are d and D, respectively. The Reynolds number of central jet (Re_c) was ranged from 50 to 3200. The Reynolds number of the coflowing air jets (Re_a) was varied from 50 to 1500. To minimize the flow perturbation of the fuel and air before going into the nozzle and the two channels, the fuel and air were passed through the honeycomb and screens. The air and fuel fluids bypassed the cyclone particle generators for performing PIV measurement. The coordinate origin was located at the center position of the downstream surface of the target blockage, where x, y, and z denote the transverse, spanwise and axial directions, respectively.

2. Flame Visualization and PIV Measurement

Images for phenomenological illustrations of the jet flames were captured by a digital camera (Model EOS 450D, Canon Inc.). The camera shutter speed was varied depending on the flame modes being captured. The maximum resolution of the digital camera was 4272 × 2848 pixels. The spatial resolution of the flame image was 0.1 mm/pixel.

A high-speed PIV system was used to measure instantaneous velocities of jet flame. The PIV system consisted of a pulsed laser, a high-speed digital camera, an electronic synchronizer, an image acquisition system, and a PIV analysis software. The pulsed laser was a dual-head diode-pumped pulsed Neodymium-doped Yttrium Lithium Fluoride (Nd:YLF) laser (Model LDY 301, Litron Laser Ltd.). The maximum repetition rate per laser head was 10 kHz. The laser pulse with wavelength 527 nm contained 10 mJ of energy at 1 kHz. The high-speed digital camera (Model Y4, Integrated Design Tools Inc.) had a complementary metal oxide semiconductor (CMOS) array sensor of active monochrome 1024 × 1024 pixels and could record up to 3000 frames per second at full resolution. A laser-light sheet expander was mounted at the exit of the laser head, so that the laser beam was expanded to a triangular light sheet with a thickness of about 0.5 mm. The particle size distribution measured by using a particle size analyzer (Model 2600C, Malvern Instruments Ltd.) ranged from 1 to 5 μm with a peak at 3.85 μm. The flow images of the jet flame were captured by high-speed digital camera. The pixel array of the camera was mapped to a physical region of 140 × 123 mm^2 so that the spatial resolution was about 136 μm/pixel. It can be operated in either single- or double-pulse mode; the double-pulse mode was adopted in the study. The time interval between two consecutive laser pulses was 100 μs. The frame rate was adjusted at 1000 image pairs per second. In order to filter out the lights emitted from the flames and allow the scattered laser light of 527 nm to enter the camera, two optical filters were adapted to the front lens. Peak transmission of the filters was about 70%. Magnesium oxide particles were seeded into the combusting flow to scatter the laser light. The pulsed laser and digital camera were triggered and synchronized by the electronic synchronizer.

Two consecutive double-exposed images were analyzed with a cross-correlation technique (Kean and Adrian, 1990) embedded in the PIV analysis software, a commercial code developed by Integrated Design Tool, Inc. In general, the software calculated the average displacement of consecutive images of the local groups of particles. The interrogation window was set to 32 × 32 pixels. The displacement of the particles in the consecutive double-exposed images was kept smaller than one-fourth of the length of the interrogation area to reduce velocity bias in the regions of large velocity gradients, as suggested by Kean and Adrian (1992). The seeding density was adjusted to keep the number of particle-image pairs per interrogation spot to no fewer than four, to prevent the measurement reliability from becoming significantly poor. The number of vectors (i.e., the grids) predetermined for the PIV analysis results was set to 46 × 46 in the median plane of the jet flame. Error check and interpolation were used to identify outliers and then regenerate interpolated values to replace the identified outliers. In general, less than 2% of spurious vectors per instantaneous field were detected and replaced by the interpolation values in this study.

3. Temperature Distribution Measurement

The temperature distributions of the jet flame were measured by a R-type thermocouple associated with a thermal recorder (Model Keithley 2750, Tektronix, Inc.). The wire diameter of the thermocouple was 125 μm. The diameter of the spark-welded bead for thermocouple was approximately 175 μm. The measuring bead protruded 2 cm away from the tip of its 2-mm-diam ceramic steam. This ceramic stem was securely fastened to an L-shaped stainless steel tube where the plug was attached. The probe was mounted on a three dimensional traversing mechanism that had a minimum step resolution of 10 μm. Because the response of the thermocouple was low, time-averaged temperatures were recorded. A convergence test was preliminarily made to determine the period for sampling the temperature data. The time-averaged values converged to nearly constant values

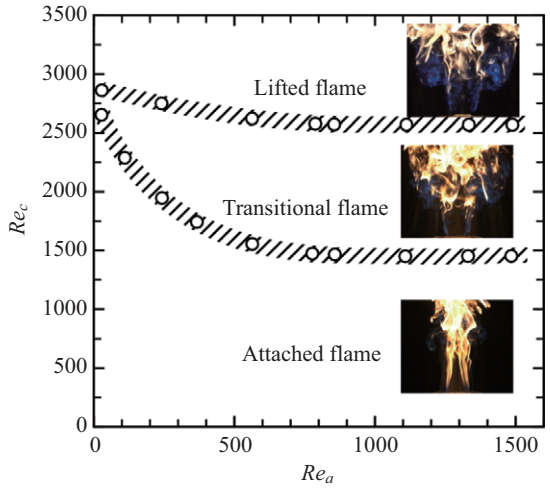

Fig. 2. Characteristic flame regime of fluidic-oscillator burner.

as the record length was more 2500 samples. In the present study, 5000 data at a sampling rate of 50 Hz were collected for each measurement. The flame was guarded by three layers of mesh screen to resolve the effects of room drafts and other disturbances due to various activities of people inside of the laboratory.

4. Uncertainty Estimation

The uncertainty estimates for each variable in the figures were based on Steele et al.'s method (Steele et al., 1993). The total uncertainty E of the variables can be found by combining systematic and random errors as $E = [B^2 + (DS_D)^2]^{1/2}$, where B is the systematic uncertainty, S_D is the standard deviation of the mean, and the degrees of freedom D are set at 2 for the 95% confidence level. The systematic uncertainty B was estimated based on the calibration data and previous test experiences. The standard deviation of the mean S_D was computed from the raw measurement data. The jet velocity was measured with a rotameter calibrated through a micro-pressure calibration system to an accuracy of 1% of the full scale. The uncertainty of the velocity components measured with the PIV technique was evaluated within 2% (Kean and Adrian, 1990). The uncertainty of the derivative vorticity was estimated to be as large as 4% (Luff et al., 1999).

III. RESULTS AND DISCUSSION

1. Characteristic Flame Behavior

Fig. 2 shows the characteristic flame modes identified in the domain of Re_c and Re_a. The typical flame images around jet exit of the fluidic-oscillator burner were included in Fig. 2. The pictures were captured in y direction at Re_a = 1334. At low central jet Reynolds number, the characteristic flame behavior is *attached flame* mode. The pulsating reacting jets issued from the side slots of the fluidic-oscillator burner form two diffusion flames which deflect toward the center plane. They merge into a turbulent reacting jet in the downstream. A dark triangular area where no flame is observed appears above the target blockage. At mediate central jet Reynolds number Re_c = 2100, the characteristic flame behavior is *transitional flame* mode. The pulsating reacting jet flames of fluidic-oscillator burner become blue diffusion flames and deflect away from the central plane. The tendency of the two diffusion flames to mergence in attached flame mode is not apparent. The blue diffusion flames start to converge toward the center plane and finally merge together. After the flames merge, the flames expand abruptly and become much wide. The abruptly widened flame is accompanied with large turbulence. In addition to the diffusion flames appearing near the burner exit, more blue flames are observed around the base. The base of the diffusion flames of the fluidic-oscillator burner exhibits an unsteady lifting and reattaching motions. At the large Reynolds number, the characteristic flame behavior is *lifted flame* mode. The blue diffusion flames lift off the burner and stand at a short distance away from the burner exit. The mergence point of the flames is lowered down. The merged flame expands transversely suddenly around that level. The flames become drastically wide with larger blue zones and stronger turbulence. The characteristic flame modes are consistent with the observation of Huang et al. (2013).

2. Time-Averaged Velocity Fields and Vorticity Contours

Fig. 3 shows the time-averaged velocity vectors and streamline patterns of the fluidic-oscillator burner flames at various central jet Reynolds numbers. The time-averaged velocity fields were obtained by averaging 5000 instantaneous velocity maps. The measurement points are dense; thus, in Fig. 3, superfluous velocity vectors were removed for clarity of presentation. The streamlines were obtained by using the shooting method.

At Re_c = 960, as shown in Fig. 3(a), the fuel and air were emitted from the pulsating fuel jet and coflowing air jets, respectively. The streamlines evolved from the exits of pulsating fuel jets go upward and gradually deflect toward central plane. A source point located at (x/W, z/W) = (-0.23, 0.56) is formed in the wake of the target blockage. Above the source point, the flow goes downstream. Beneath the source point, the flow reverses toward upstream direction, and forms a reverse flow region. The magnitudes of velocity vectors in reverse flow region are smaller than those in downstream region. For all streamlines evolved from exit of coflowing air jets, most streamlines go upward and few streamlines are deflected outward (away from the central plane). As Re_c increases, as shown in Figs. 3(b) and (c), the flow characteristics behave similarly to Fig. 3(a). The impingement intensity of pulsating jets on coflowing jets is increased so that more streamlines evolved from the exits of coflowing air jets deflect outward. The source points formed in the wake of the target blockage locate at (x/W, z/W) = (0.06, 0.77) and (x/W, z/W) = (-0.21, 0.94) in Figs. 3(b) and (c), respectively. As Re_c increases, the source point moves upward and the reverse flow region enlarges.

The time-averaged vorticity contours of the fluidic-oscillator burner at various flame modes are shown in Fig. 4. The isovorticity contours are computed from the time-averaged velocity

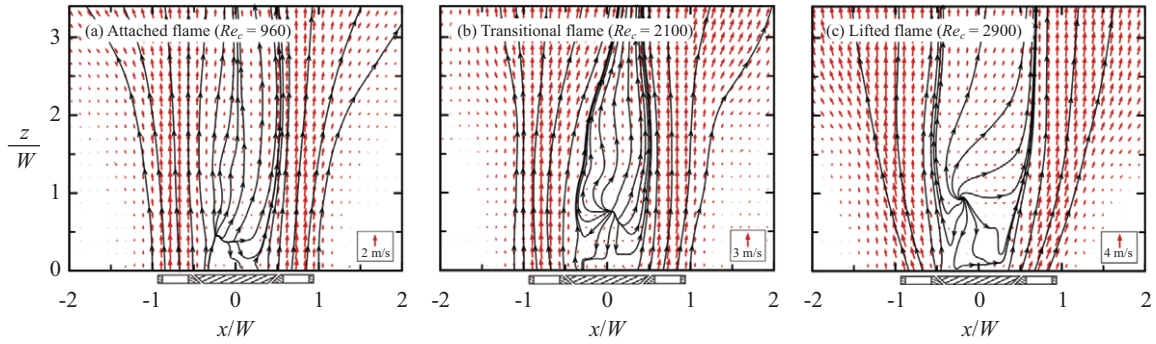

Fig. 3. Time-averaged velocity vectors and streamline patterns in symmetry plane of fluidic-oscillator burner. Re_a = 1344.

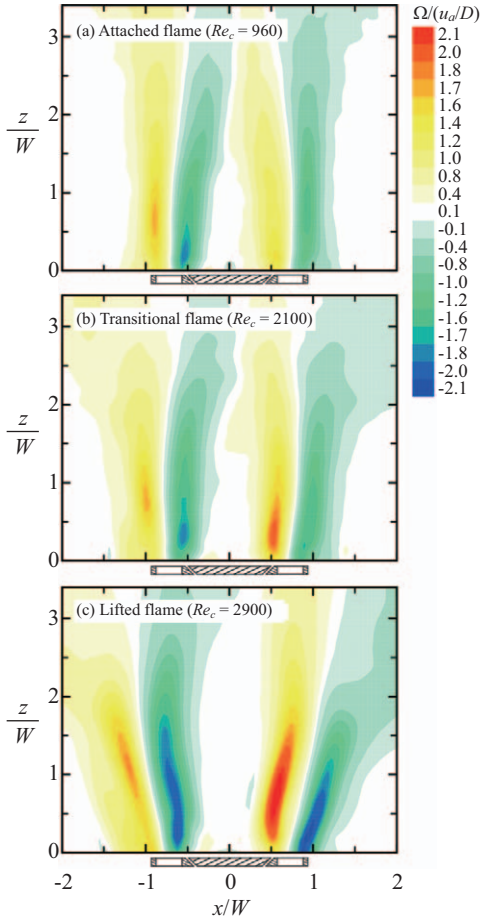

Fig. 4. Time-averaged vorticity contours in symmetry plane of fluidic-oscillator burner. Re_a = 1344.

fields shown in Fig. 3. The vorticity Ω is normalized by u_a/D for the range $-2.1 \le \Omega/(u_a/D) \le 2.1$. Positive vorticity represents a counterclockwise rotation, while negative vorticity represents a clockwise rotation. In Fig. 4(a), for the attached flame mode, the vorticity contours are almost mirror-reflection about the central plane (*x*-*y* plane). Two adjacent vorticity-concentrated areas with opposite signs are formed around the region where the pulsating fuel jet interacts with the coflowing air jets. The interaction between pulsating fuel jet and coflowing air jets induces large shear effect so that the distinct vorticity-concentrated areas are formed. The vorticity value is nearly zero in the wake region of the target blockage.

Figs. 4(b) and (c) show the time-averaged vorticity contours in the transitional and lifted flame modes, respectively. These vorticity contours present a pattern similar to that of the attached flame mode shown in Fig. 4(a); however, the areas and values of the adjacent vorticity-concentrated areas are increased with increasing central jet Reynolds number. For example, the maximum value of the vorticity contours in attached flame mode (Fig. 4(a)) is about 1.7, while the peak value of the vorticity contours in the lifted flame mode (Fig. 4(c)) is about 2.1. Because the increase of pulsating fuel jet velocity enhances shear effect on the interaction region between the pulsating jet and coflowing air jets, therefore the vorticity values increase. The increase of pulsating jet velocity also creates a large impingement effect on the coflowing air jets, the coflowing air jets hence deflect toward transverse direction (i.e., *x* or -*x* directions), the vorticity-concentrated area therefore expands.

3. Velocity Profiles and Turbulence Intensities

The transverse distributions of normalized axial velocity (v/u_a) and axial turbulence intensity ($\sqrt{\overline{v'^2}}/u_a$) of the fluidic-oscillator burner at $z/W = 0.5$ and $z/W = 3.0$ are shown in Figs. 5 and 6, respectively. The axial level chosen at $z/W = 0.5$ located near exit of flames, whereas that chosen at $z/W = 3.0$ located above mergence point of the flames. The fluctuation velocity ($\sqrt{\overline{v'^2}}$) is the root-mean-square value of the instantaneous axial velocity with the local-time-averaged velocity subtracted. Those results are obtained over 5000 instantaneous velocity fields.

Fig. 5 shows the transverse distributions of normalized axial velocity and axial turbulence intensity of fluidic-oscillator burner at $z/W = 0.5$. In Fig. 5(a), the transverse distributions of axial velocity for the three flame modes show the dual-hump profiles. A velocity hump typically represents a reacting jet flow. It is formed by the reacting jet combining the pulsating fuel jet and coflowing air jets. As the central jet Reynolds number increases, the peak values and the transverse distance between the

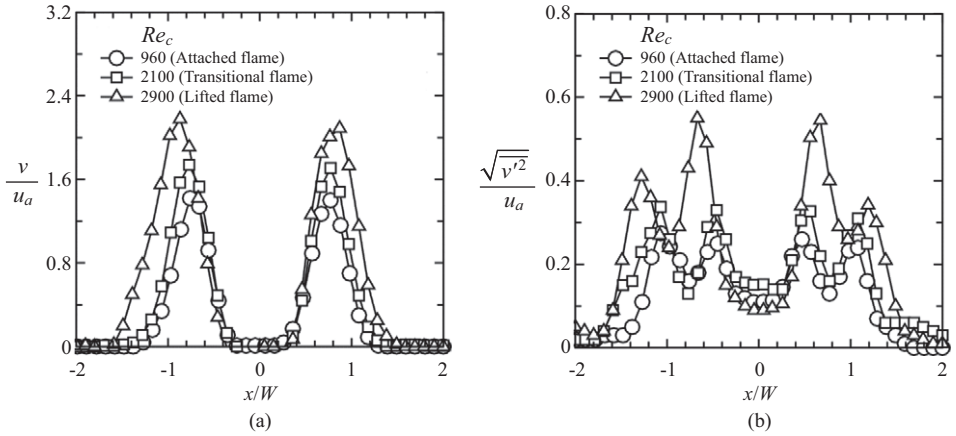

Fig. 5. Transverse distributions of (a) axial velocity and (b) turbulence intensity in different flame modes at $z/W = 0.5$. $Re_a = 1344$.

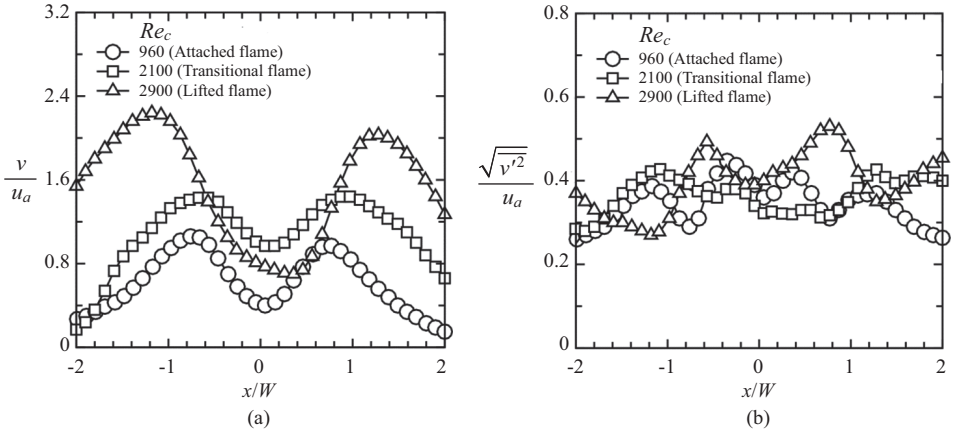

Fig. 6. Transverse distributions of (a) axial velocity and (b) turbulence intensity in different flame modes at $z/W = 3.0$. $Re_a = 1344$.

dual humps of the velocity profiles increase. The peak values and transverse distance between the dual humps of the velocity profiles in the lifted flame mode are larger than those in transitional and attached flame modes. The troughs within two humps are located around the central axis. The velocities values at the trough are almost zero because of the flows are within the reverse flow region. In Fig. 5(b), the distributions of axial turbulence intensity at the three flame modes show four humps. Two humps of the turbulence intensity distributions exhibiting on both sides of the center axis are the typical profile of a reacting jet flow. The inner hump (near central axis) is the shear layer induced by pulsating jet and coflowing air jets, while the outer hump is the shear layer induced by coflowing air jets and ambient air. The peak value of turbulence intensity profiles increases with increasing central jet Reynolds number. The lifted flame mode has larger peak turbulence intensity than the attached and transitional flame modes. In the lifted flame mode, the peak value of the inner hump is significantly larger than that of the outer hump. However, in the attached flame mode, the peak values of the inner and outer humps are nearly the same. Because the pulsating fuel jet velocity in lifted flame mode is large, the shear effect between the pulsating fuel jet and coflowing air jets is large. Therefore, a peak value of the inner hump is drastically larger than that of the outer hump.

Fig. 6 shows the transverse distributions of normalized axial velocity and axial turbulence intensity of different flame modes at $z/W = 3.0$. Their respective profiles exhibit characteristics similar to those shown in Fig. 5. As the axial level increases from $z/W = 0.5$ to $z/W = 3.0$, the interaction of pulsating fuel jet and coflowing air jets causes entrainment, thus spread toward outer direction. Therefore, as the axial level increases, the peak value of the normalized axial velocity decreases and the transverse distance between the dual humps increases, as shown in Fig. 6(a). The velocity values of the trough within two humps increase because the flow above the source point directs upward. The spread of the reacting jets toward outer direction induces large fluctuation, so that the profiles of the axial turbulence intensity increase, as shown in Fig. 6(b). The spread also reduces the momentum of the reacting jets, and then reduces the shear effect between the fuel jet and air jets. Therefore, the peak values of the axial turbulence profiles decrease.

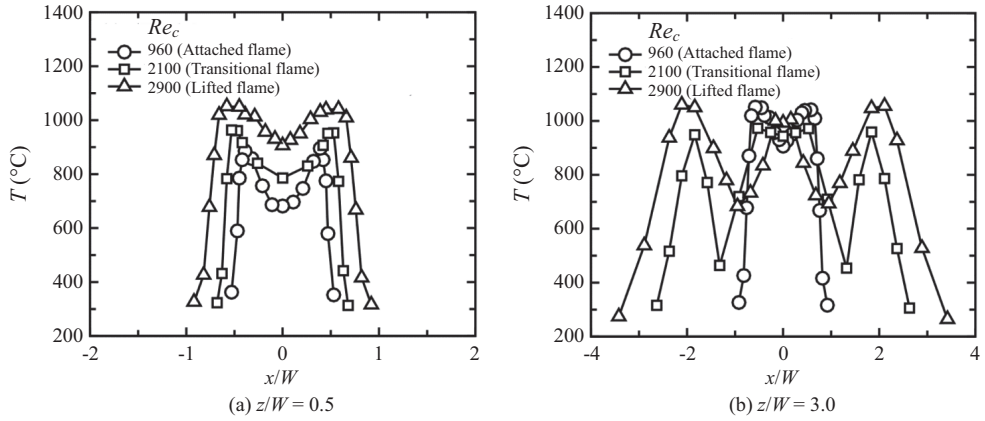

Fig. 7. Transverse temperature distributions in different flame modes. Re_a = 1344. (a) z/W = 0.5, (b) z/W = 3.0.

4. Temperature Distributions

Fig. 7 shows the transverse temperature distributions in different flame modes at z/W = 0.5 and z/W = 3.0. At z/W = 0.5, as shown in Fig. 7(a), the pulsating reacting jets are issued from the side slots of the fluidic-oscillator burner form two diffusion flames so that the temperature distributions exhibit two humps. At Re_c = 960 (attached flame mode), the peak value of temperature profile is around 900°C. A trough located within two humps is formed around the central axis because no flame appears in the near wake of the target blockage. The temperature value of the trough is around 680°C. As the central jet Reynolds number increases, the temperature values of the humps and trough increase, so that those in lifted flame mode are higher than those in attached flame mode. For example, at Re_c = 2900 (lifted flame mode) the peak value of the temperature profile is around 1070°C. The temperature value of the trough is around 900°C. At z/W = 3.0, as shown in Fig. 7(b), the temperature distributions are wider than those at z/W = 0.5 because the reacting jets expand transversely with increasing axial distance. The temperature distribution in lifted flame mode is wider than that in attached flame or transitional flame mode. The pulsating reacting jets issued from the side slots of the fluidic-oscillator burner deflect toward the center plane and merge into a turbulent reacting jet after z/W > 2.3, therefore the temperature value of the trough increases.

5. Velocity and Temperature Trajectories

The jet flame trajectory is identified by tracking the maximum velocities and temperatures. To study the jet flame trajectory of the fluidic-oscillator burner, the velocity and temperature trajectories are measured from the transverse distributions of axial velocities and temperatures. The velocity trajectories of the fluidic-oscillator burner at different flame modes are shown in Fig. 8. The velocity trajectory of the jet flame is the loci of the maximum axial velocity in the transverse distributions (as shown in Figs. 5 and 6) at various axial distances. The velocity trajectories of the attached and transitional flame modes direct upward and almost collapse together. However, the velocity

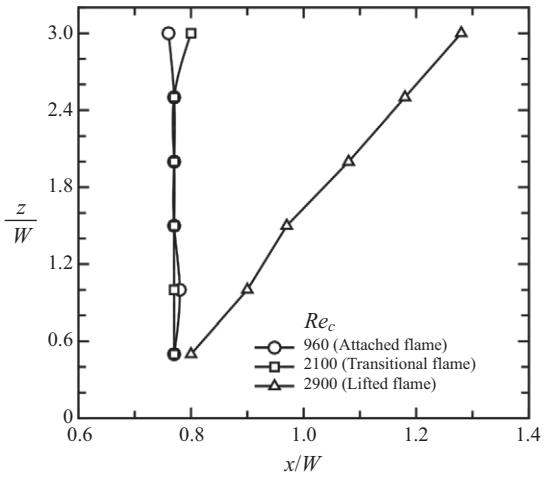

Fig. 8. Velocity trajectories of fluidic-oscillator burner. Re_a = 1344.

trajectory of the lifted flame mode penetrates into positive transverse direction (+x) with increasing axial distance. The temperature trajectories of the fluidic oscillator burner at various flame modes are shown in Fig. 9. The temperature trajectory of the jet flame is the loci of the maximum temperature in the transverse direction (as shown in Fig. 7) at various axial distances. The temperature trajectories of the attached and transitional flame modes direct upward. The temperature trajectory of the attached flame mode locates more close to the central jet axis when compared to the attached flame mode. The temperature trajectory of the lifted flame mode directs upward at z/W < 1.4 and penetrates into transverse direction with increasing axial distance at z/W > 1.4. The temperature trajectories locate inner the velocity trajectories at the attached and transitional flame modes. However, the temperature trajectory locates approximately outer the velocity trajectory at the lifted flame mode.

IV. CONCLUSIONS

The characteristic flame behavior, time-averaged velocity fields, and transverse temperature distributions of the fluidic-

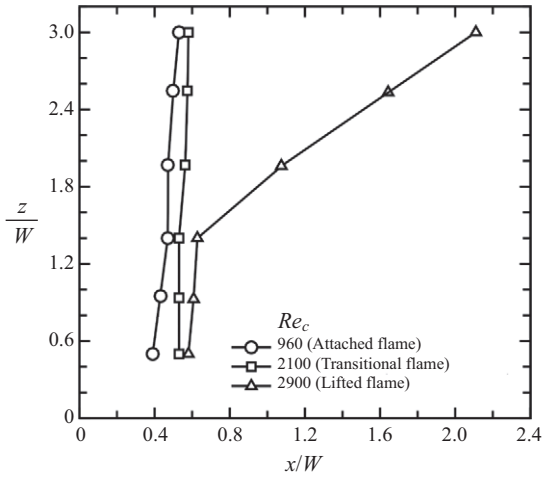

Fig. 9. Temperature trajectories of fluidic-oscillator burner. Re_a = 1344.

oscillator were studied using the flame visualization method, the high-speed PIV technique, and temperature measurement. The conclusions described below were drawn from the experimental results.

(1) Three characteristic flame regimes were observed in the domain of Re_c and Re_a, which can be respectively described as the *attached flame*, *transitional flame*, and *lifted flame*.
(2) In the time-averaged velocity field, a source point is formed in the wake of the target blockage. Above the source point, the flow goes downstream direction. Beneath the source point, the flow reverses toward upstream direction and forms a reverse flow region. As Re_c increases, the source point moves upward, therefore the reverse flow region enlarges.
(3) Two adjacent vorticity-concentrated areas with opposite signs are formed around the region where the pulsating fuel jet interacts with the coflowing air jets. The vorticity value is nearly null in the wake region of the target blockage. The vorticity values increase with increasing Re_c because the increase of pulsating fuel jet velocity enhances shear effect on the interaction region between the pulsating jet and coflowing air jets.
(4) The transverse distributions of axial velocity of the three flame modes show the dual-hump profiles. The peak values and transverse distance between the dual hump of the velocity profiles in the lifted flame mode are larger than those in transitional and attached flame modes. The lifted flame mode has larger peak turbulence intensity than the attached and transitional flame modes.
(5) The pulsating reacting jets issued from the side slots of the fluidic-oscillator burner form two diffusion flames so that the temperature distributions exhibit two humps. The temperature distribution is wider and the peak temperature is larger in lifted flame mode when compared to attached flame or transitional flame mode.
(6) The temperature and velocity trajectories of the attached and transitional flame modes direct upward, whereas those of the lifted flame modes penetrate into transverse direction. The temperature trajectories locate inner the velocity trajectories ~~at~~ in the attached and transitional flame modes. However, the temperature trajectory locate approximately outer the velocity trajectory at the lifted flame mode.

NOMENCLATURE

b	width of inclined channel of fluidic-oscillator burner
d	width of nozzle exit
D	width of coflow air jets
Re_a	jet Reynolds number based on width of coflow air jets D
Re_c	jet Reynolds number based on width of nozzle exit d
s	span length of inclined channel of fluidic-oscillator burner, 165 mm
T	flame temperature
u_a	averaged exit velocity of coflowing air jets
u_c	averaged exit velocity of central jet
v	time-averaged axial velocity
$\sqrt{v'^2}$	root-mean-square value of the instantaneous axial velocity
W	downstream width of target blockage, 35 mm
x	Cartesian coordinate in transverse direction
y	Cartesian coordinate in spanwise direction
z	Cartesian coordinate in axial axis
v_a	kinematic viscosity of air jet
v_c	kinematic viscosity of fuel jet
Ω	vorticity flow field ($= \frac{\partial \overline{v}}{\partial x} - \frac{\partial \overline{u}}{\partial z}$)

Subscripts

a	coflowing air jets
c	central jet

REFERENCES

Deo, R. C., J. Mi and G. J. Nathan (2007). The influence of nozzle aspect ratio on plane jets. Experimental Thermal and Fluid Science 31, 825-838.

Gad-el-Hak, M., A. Pollard and J.-P. Bonnet (1998). Flow Control: Fundamentals and Practices, Lecture Notes in Physics, Springer-Verlag, Berlin, 335-429.

Gutmark, E. and I. Wygnanski (1976). The planar turbulent jet. Journal of Fluid Mechanics 73, 465-495.

Huang, R. F. and K. T. Chang (2004). Oscillation frequency in wake of a vee-gutter. Journal of Propulsion and Power 20(5), 871-878.

Huang, R. F. and K. T. Chang (2005). Fluidic oscillation influences on vee-shaped bluff-body flow. AIAA Journal 43(11), 2319-2328.

Huang, R. F. and K. T. Chang (2007). Evolution and turbulence properties of self-sustained transversely oscillating flow induced by fluidic oscillator. Journal of Fluids Engineering 129(8), 1038-1047.

Huang, R. F., H. F. Yang and C. M. Hsu (2013). Flame behavior and thermal structure of combusting nonpulsating and pulsating plane jets. Journal of Propulsion and Power 29(1), 114-124.

Huerre, P. and P. A. Monkewitz (1985). Absolute and convective instabilities in free shear layers. Journal of Fluid Mechanics 159, 151-168.

Hussain, A. K. M. F. and A. R. Clark (1977). Upstream influence on the near field of a plane turbulent jet. Physics of Fluids 20(9), 1416-1426.

Keane, R. D. and R. J. Adrian (1990). Optimization of particle image velocimeters part I: double pulsed systems. Measurement Science and Technology

1, 1202-1215.
Keane, R. D. and R. J. Adrian (1992). Theory of cross-correlation analysis of PIV images. Applied Scientific Research 49, 191-215.
Lin, C. K., F. B. Hsiao and S. S. Sheu (1993). Flapping motion of an impinging jet on a V-shaped plate. Journal of Aircraft 30(3), 320-325.
Luff, J. D., T. Drouillard, A. M. Rompage, M. A. Linne and J. R. Hertzberg (1999). Experimental uncertainties associated with particle image velocimetry (PIV) based vorticity algorithms. Experiments in Fluids 26, 36-54.
Mi, J. and G. J. Nathan (2005). Statistical analysis of the velocity field in a mechanical precessing jet flow. Physics of Fluids 17, 1-17.
Namar, I. and M. V. Otugen (1988). Velocity measurements in a plane turbulent air jet at moderate Reynolds numbers. Experiments in Fluids 6(6), 387-399.
Quinn W. R. (1992). Turbulent free jet flows issuing from sharp-edged rectangular slots: the influence of slot aspect ratio. Experimental Thermal and Fluid Science 5(2), 203-215.
Sato H. (1960). The stability and transition of a two-dimensional jet. Journal of Fluid Mechanics 7, 53-80.
Steele,W. G., R. P. Taylor, R. E. Burrell and H. W. Coleman. (1993). Use of previous experience to estimate precision uncertainty of small sample experiments. AIAA Journal 31(10), 1891-1896.
Thomas, F. O. and V. W. Goldschmidt (1986) Structural characteristics of a developing turbulent plane jet. Journal of Fluid Mechanics 163, 227-256.
Tippetts, J. R., H. K. Ng and J. K. Royle (1973). An oscillating bi-stable fluid amplifier for use as a flowmeter. Journal of Fluid Control (Fluidics Quarterly) 5, 28-42.
Wang, H., S. B. M. Beck, G. H. Priestman and R. F. Boucher (1998). A remote measuring flow meter for petroleum and other industrial applications. Measurement Science and Technology 9, 779-789.
Yamasaki, H. and S. Honda (1981). A unified approach to hydrodynamic oscillator type flowmeters. Journal of Fluid Control 13, 1-17.
Yamamoto, K., F. Hiroki and K. Huodo (1999). Self-sustained oscillation phenomena of fluidic flowmeters. Journal of Visualization 1, 387-396.
Yang, H. F., C. M. Hsu and R. F. Huang (2014a). Controlling plane-jet flame by a fluidic oscillation technique. Journal of Engineering for Gas Turbines and Power 136, 041501.
Yang, H. F., C. M. Hsu and R. F. Huang (2014b). Flame behavior of bifurcated jets in a V-shaped bluff-fody burner. Journal of Marine Science and Technology 22 (5), 606-611.
Zaman K. B. M. Q. (1999). Spreading characteristics of compressible jets from nozzles of various geometries. Journal of Fluid Mechanics 383, 197-228.